CORROSION SCIENCE AND TECHNOLOGY, Vol.23, No.2(2024), pp.166~178 pISSN 1598-6462 / eISSN 2288-6524
[Review Paper] DOI: https://doi.org/10.14773/cst.2024.23.2.166

# Localized Corrosion Resistance and Microstructural Changes in UNS N07718 Alloy After Solution Heat Treatment

**Yoon-Hwa Lee[1,2], Jun-Seob Lee[1,2,†], Soon il Kwon[3], Jungho Shin[3], and Je-Hyun Lee[1,2]**

[1]*School of Materials Science and Engineering, Changwon National University, Changwondaehak-ro, Changwon, 51140, South Korea*
[2]*Department of Materials Convergence and System Engineering, Changwon National University, Changwondaehak-ro, Changwon, 51140, South Korea*
[3]*R&D Center, SeAH CSS corporation, Jeokhyun-ro, Changwon, 51708, South Korea*
(Received February 21, 2024; Revised March 19, 2024; Accepted March 20, 2024)

The localized corrosion resistance of UNS N07718 alloy was investigated after solution heat treatment. When the alloy was heat-treated at 1050 °C for 2.5 hours, it experienced an increase in average grain diameter, a reduction in grain boundary area, and the dissolution of delta phases along grain boundaries. Additionally, primary metallic nitrides (MN) and metallic carbides (MC), enriched with either Ti or Nb, were identified and exhibited a random distribution within the microstructures. Despite the solution heat treatment, the composition, diameter, and abundance of MNs and MCs remained relatively consistent. The critical pitting temperature (CPT), as determined by the ASTM G48-C immersion test, revealed similar values of 45 °C for both treated and untreated alloys. However, a decrease in maximum pit depth and corrosion rate was observed after the solution heat treatment. The microstructural changes that occurred during the heat treatment and their potential implications were discussed to understand the influence of the solution heat treatment.

***Keywords:*** *Inconel, Heat treatment, Corrosion, Carbide*

## 1. Introduction

The precipitation-hardened nickel-based UNS N07718 alloy is widely used owing to its strength and resistance to corrosion in aqueous environments, including oil fields, marine, and high-temperature applications [1-3]. It is particularly effective in marine environments where components like fasteners, bolts, and nuts are susceptible to localized corrosion [4,5].

The localized corrosion resistance of alloys is strongly influenced by their microstructure. This is because localized corrosion in alloys often initiates in metallurgically heterogeneous regions, where the electrochemical reactivity between different microstructures is not uniform. Factors such as chemical composition segregation, grain orientation, grain boundaries, precipitates, and secondary phases contribute to this heterogeneity [6,7]. The localized corrosion behavior of UNS N07718 is similarly linked to its heterogeneous microstructures. Interestingly, the study of localized corrosion behavior in UNS N07718 has only recently emerged. Lee et al. suggested that the localized corrosion of the age-hardened alloy initiates at the interface between primary carbide phases and the austenitic substrate due to the electrochemical energy difference [8,9]. The carbide phases, composed of MC (M = Ti or Nb), form during solidification at relatively high temperatures in liquid phases. These carbide phases are randomly distributed on the austenitic phases, with diameters ranging from approximately 1 to 10 μm [8]. By employing a Kelvin probe force microscope, the researchers examined the contact potential difference (CPD) between carbide phases and substrate phases. They suggested that the higher CPD values of MC compared to the substrate resulted in the initiation site of localized corrosion in UNS N07718 [9].

In order to maintain the desirable properties of the UNS N07718 alloy, it is essential to properly heat treat the material for maintenance purposes. The heat treatment of the alloy typically involves a two-step sequence consisting of a solution and age-hardening heat treatment [10]. When

†Corresponding author: junseoblee@changwon.ac.kr
Yoon-Hwa Lee: Graduate student, Jun-Seob Lee: Professor, Soon il Kwon: Researcher, Jungho Shin: Researcher, Je-Hyun Lee: Professor

the alloy is cast, it undergoes a solution heat treatment to reduce segregation and dissolve undesirable secondary phases, such as the delta (δ) phase at grain boundaries [11]. Following the solution heat treatment, the UNS N07718 alloy is hardened by the precipitation of secondary phases, such as gamma prime (γ') and gamma double prime (γ") phases, within the austenitic grains [12]. A sufficient solution heat treatment is crucial, as it significantly impacts the mechanical properties [10,13] and localized corrosion resistance [13-15] of the alloy. Thus, investigating the changes in localized corrosion resistance after each stage of the solution heat treatment and precipitation hardening treatment is vital for assessing the alloy's lifespan and improving its corrosion resistance.

Solution heat treatments were applied to UNS N07718 specimens of varying chemical compositions. Subsequent evaluations assessed the mechanical properties and resistance behaviors to sulfide stress cracking, galvanically induced hydrogen stress cracking, stress corrosion cracking, and hydrogen embrittlement under different age-hardening heat treatment conditions. These investigations facilitated a comparison between the as-hot-rolled and age-hardened UNS N07718 specimens. Notably, a comparative analysis focusing on localized corrosion resistance before and after the solution heat treatment was not conducted [13]. Rebak et al. assessed the localized corrosion resistance of UNS N07718 alloys by evaluating the corrosion potential, corrosion rate, and critical crevice temperature under various aging heat treatments. However, their study did not review the impact of these heat treatments on the composition and distribution of carbides within the alloys, nor its subsequent effect on localized corrosion resistance at different stages of heat treatment [14]. Valle et al. examined the impact of solution heat treatment on the localized corrosion resistance of UNS N07718 alloy in a chloride solution, using potentiostatic polarization. Their conclusion indicated an improvement in localized corrosion resistance, as the anodic current flows recorded during polarization were higher for as-hot-rolled alloys compared to those subjected to solution heat treatment [15]. However, with an applied potential of 1.5 $V_{SCE}$, the collected anodic current likely includes both transpassive current and oxygen generation contributions. This suggests that comparing the localized corrosion resistance of alloys post-heat treatment may not provide a comprehensive understanding of the effect of treatment on their localized corrosion resistance.

The authors also reported that the critical pitting temperature of UNS N07718 alloy, after the ageing heat treatment, was determined to be 45 ºC. This determination was made through mass loss measurements during immersion testing in a 6 wt% $FeCl_3$ solution with the addition of 1 wt% HCl. In addition, electrochemical techniques were employed to assess the localized corrosion resistance by comparing changes in pitting potential values at different solution temperatures, ranging from room temperature to 80 ºC, in NaCl solutions [9]. Surprisingly, this evaluation of the alloy's localized corrosion resistance represented the first set of fundamental data, which was typically absent from alloy suppliers' data sheets. This information proved valuable for gaining insight into the localized corrosion resistance of UNS N07718 alloy. However, it was challenging to find information on how the localized corrosion resistance of the as-hot-rolled UNS N07718 is affected after solution treatment. Therefore, this study investigated the effect of solution heat treatment on the localized corrosion resistance of the as-hot-rolled UNS N07718 alloy. The study examined how the solution heat treatment influences the changes in the alloy's microstructure. The immersion and electrochemical tests were carried out to evaluate the localized corrosion resistance after the heat treatment.

## 2. Experimental

### 2.1 Materials preparation and surface analysis

The material used in this study was prepared from the UNS N07718 alloy rod, and its composition is given in Table 1. The sample had a diameter of 26 mm and a length of 300 mm. The samples were divided into two types based on heat treatment. One of the as-hot-rolled rods remained in its original condition, while the other rod underwent solution heat treatment at 1050 ºC for 2.5 hours, followed by water quenching.

The two types of samples were cut into 5 mm-thick specimens and then ground using SiC papers down to 3000 grit. After mirror-polishing the specimens with a 1 μm diamond suspension, they were etched for 3 minutes using Kalling's No.2 reagent (5 g $CuCl_2$ + 100 mL HCl + 100 mL ethanol). The surfaces of the etched specimens

**Table 1. Chemical composition of UNS N07718**

| | C | Ni | Cr | Mo | Ti | Nb | Fe |
|---|---|---|---|---|---|---|---|
| wt% | 0.05 | 53.3 | 18.4 | 2.9 | 0.9 | 5.2 | Bal. |

were observed under an optical microscope. Grain size measurements were conducted using ASTM E112–96 [16]. An image analyzer software was utilized to determine the size of particles, and the frequency distribution for particle size was determined. Microstructure analyses were performed using a scanning electron microscope (JSM-7900F, Jeol), including back-scattered electron image (BSE), secondary electron image, and energy dispersive spectroscopy (EDS).

The mirror-polished, as-hot-rolled UNS N07718 was prepared after etching for 100 seconds using Kalling's No.2 reagent. Scanning Kelvin Probe Force Microscopy (SKPFM) was performed using an atomic force microscope (XE-100, Park Systems) in electrostatic force microscope mode. A Si cantilever with a Cr/Pt coating (Multi 75E, Park Systems) was used. The scan area was 30 × 30 μm² with a scan rate of 0.1 Hz.

### 2.2 Immersion test

The immersion test was conducted following ASTM G-48 C-method [17]. The experimental solution consisted of 6 wt% $FeCl_3$ + 1 wt% HCl, and the immersion time was set at 72 hours. The two types of samples were cut into 5 mm-thick specimens and ground using 100-grit SiC paper. After grinding, the samples underwent ultrasonic rinsing with deionized water, ethanol, and acetone for 5 minutes. The mass of the specimens was measured before and after the immersion test. Both samples were immersed at 35 ºC, and when there was no mass loss observed, the temperature was increased by 5 ºC to proceed with the experiment. Following each solution temperature during the immersion test, the corrosion rate was calculated in mpy (miles penetration per year) based on the mass loss of the two types of samples. A single specimen was placed in a test container at each solution temperature. After raising the test temperature, new specimens were employed alongside fresh solutions. Furthermore, the immersion test was conducted a minimum of five times for both types of UNS N07718. After the immersion test, the specimens were examined using an optical microscope and a confocal laser microscope (VK-X1000, Keyence). The analysis of the specimens was conducted using the multiple-file-analyzer software, which measured the average, maximum, and minimum depth of corrosion, as well as the corroded areas.

### 2.3 Electrochemical experiments

The electrochemical measurements were conducted using a three-electrode system. The working electrodes were two types of UNS N07718 alloys. The UNS N07718 specimens were soldered to Cu wire using Sn and subsequently impregnated in epoxy resin. The working electrode surface was ground using 600-grit SiC paper. The counter electrode consisted of a dense carbon rod with a surface area of 40 $cm^2$. The reference electrode used was an Ag/AgCl electrode in saturated KCl (silver/silver chloride, Ag/AgCl in saturated KCl, SSE). The area of the exposed specimen was controlled to approximately 0.2 $cm^2$ using epoxy adhesive.

The electrolyte used was a solution containing 25 wt% NaCl and 0.5 wt% acetic acid to effectively show the difference in corrosion resistance under severe environemt, maintained at 50 ºC using a circulator water bath (bath circulator, Jelo Tech). The UNS N07718 electrode was polarized using a potentiostat (SP-200, Biologic). Transient electrode potential was measured for 3600 seconds before performing the potentiodynamic polarization test. The potentiodynamic polarization test was conducted in the potential range of −0.19 to 0.6 $V_{SSE}$, at a scan rate of 0.167 mV $s^{-1}$. In all electrochemical tests, reproducibility was ensured by conducting the experiments at least three times with the two types of UNS N07718.

## 3. Results and Discussion

Fig. 1 shows optical microscopic images of UNS N07718 surfaces: (a) before and (b) after the solution heat treatment. The microstructure of the alloy mostly comprises an austenite (γ) phase. It also contains a few micrometer-sized, polygonal-shaped particles that are

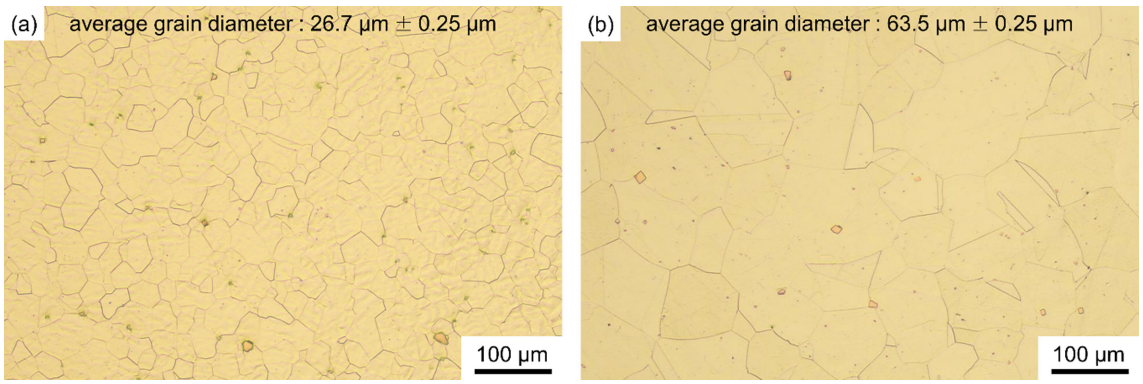


**Fig. 1. Optical microscopic images of (a) as-hot-rolled (b) solution heat-treated UNS N07718 alloys**

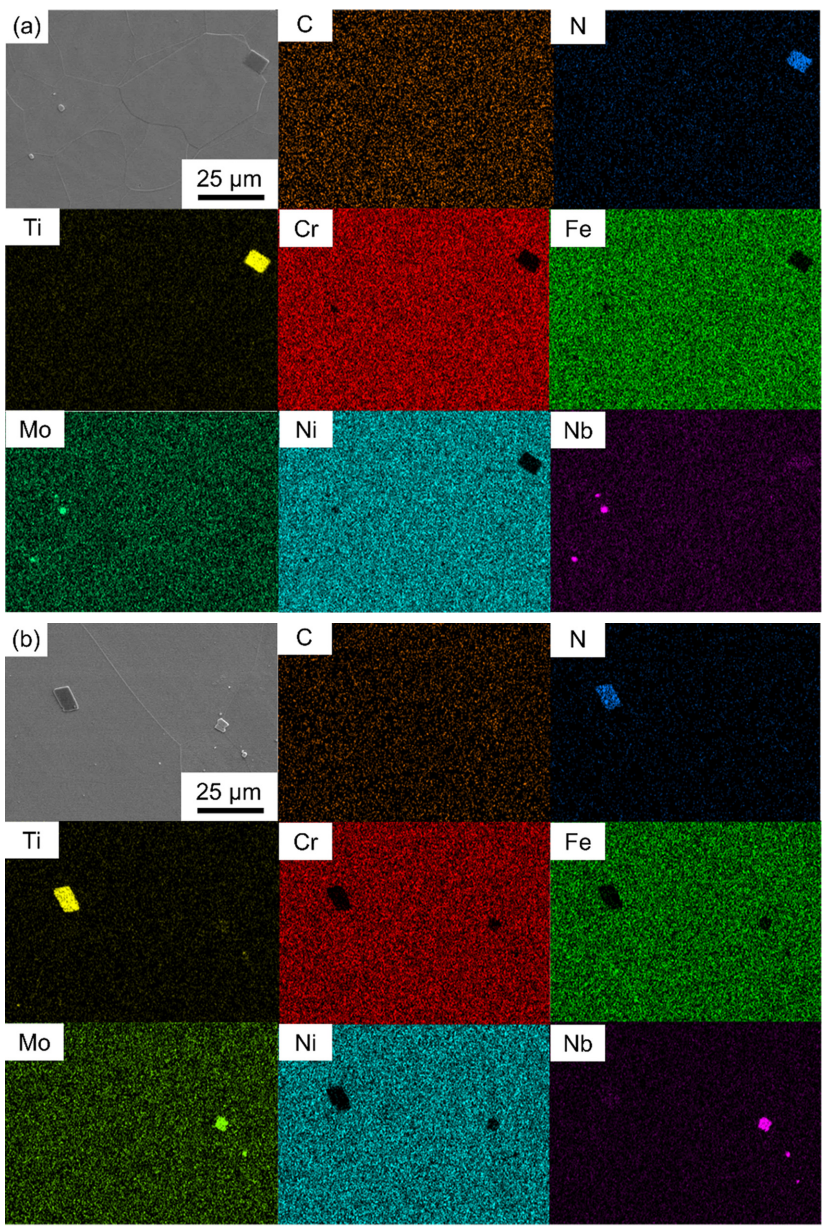


**Fig. 2. EDS elemental mapping images of (a) as-hot-rolled (b) solution heat-treated UNS N07718 alloys**

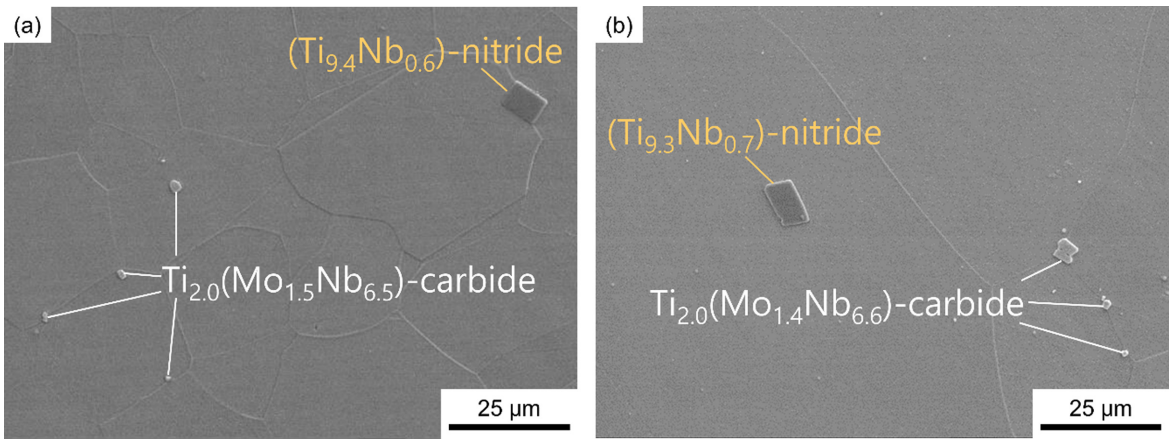


**Fig. 3. Secondary electron images and the stoichiometry of the MCs in (a) as-hot-rolled (b) solution heat-treated UNS N07718 alloys**

distributed randomly, irrespective of the heat treatment process. Upon heat treatment of the as-hot-rolled alloy, the average grain diameter in the austenitic structures increased from 26.7 μm to 63.5 μm. It is suggested that grain growth is due to the solution heat treatment at 1050 °C, which is within the preferred temperature range of 900 to 1050 °C to avoid the δ phase and allow recrystallization of the grains in UNS N07718 [18-21].

Fig. 2 presents secondary electron images and energy-dispersive spectroscopic elemental mapping images of (a) as-hot-rolled and (b) solution heat-treated UNS N07718 alloy. The alloy substrates primarily consist of Cr, Fe, and Ni, while the particles distributed on the substrate are composed of Ti, Mo, Nb and N, regardless of the solution heat treatment. The darker and brighter grey particles relative to the substrate, with diameters of approximately 10 μm or 1 μm respectively, mainly consist of Ti or Nb-Mo. Since elements lighter than sodium (with atomic number 11) [22] are difficult to detect through spectra using SEM-EDS analysis, the C content in the EDS elemental images could not be identified. Previous studies have reported that the metallic nitrides (MN) and primary metallic carbides (MC) formed during solidification are complex TiN nitrides or Nb(-Mo)C carbides [23-25]. As a result, the distributed Ti or Nb-Mo particles displayed in Fig. 2 are considered to be MN nitrides and MC carbides.

Fig. 3 presents secondary electron images illustrating the stoichiometry of the MNs and MCs in (a) as-hot-rolled and (b) solution heat-treated UNS N07718 alloy, as determined by SEM-EDS point analysis. The chemical composition of the MNs and MCs can be categorized into Ti-rich nitrides and Nb-rich carbides, which correspond to the larger and smaller particle diameters, respectively. The stoichiometry of the MNs and MCs remains largely unchanged even after heat treatment, suggesting that the solution annealing at 1050 °C for 2.5 hours has minimal influence on the compositional changes of the MNs and MCs in UNS N07718 alloy. It has been reported that the eutectic reaction from the liquid phase (L) to gamma phase (γ) + TiN (MN) or Nb/TiC (MC) in the UNS N07718 alloy occurs below 1250 °C [23-25]. Therefore, it is considered that the solution heat treatment at 1050 °C for 2.5 hours is insufficient for dissolving or changing the chemical compositions of the MNs and MCs.

Fig. 4 illustrates the frequency distribution of particle diameters for the (a) as-hot-rolled and (b) solution heat-treated UNS N07718 alloy. The particle distributions display exponential decreases from 0 to 11 μm, irrespective of the heat treatment. Over 90% of particles possess a diameter of less than 2 μm, while approximately 1% have a diameter exceeding 10 μm. Since the relatively large and small particle diameters are identified as Ti-nitride and Nb-carbide, respectively, in Fig. 3, it can be inferred that most of the particles present in the alloy are Nb-carbides.

Table 2 presents the average corrosion rate of UNS N07718 alloy after a 72-hour immersion test in a 6 wt% $FeCl_3$ + 1 wt% HCl solution. The corrosion rate is calculated as follows [26] :

$$\text{corrosion rate, mpy (mils penetration per year)} = \frac{534\,W}{D \cdot A \cdot T} \quad (1)$$

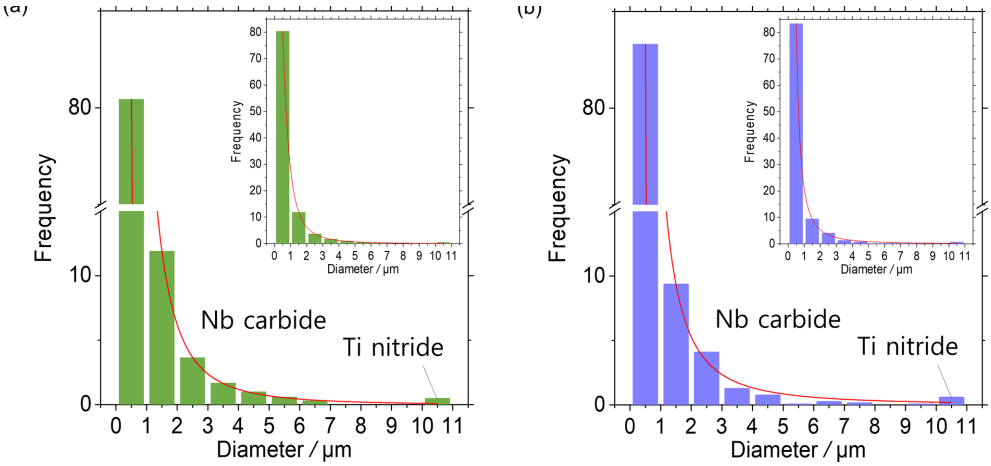


**Fig. 4. Frequency distribution for particle size of (a) as-hot-rolled (b) solution heat-treated UNS N07718 alloys**

**Table 2. Corrosion rate (mils penetration per year, mpy) after the immersion in 6 wt% $FeCl_3$ + 1 wt% HCl of as-hot-rolled and solution heat-treated UNS N07718 alloys**

| Temperature (°C) | 40 | 45 | 50 | 55 |
|---|---|---|---|---|
| As-hot-rolled | 0.00 | 1.82 ± 1.68 | 9.24 ± 7.20 | 95.20 ± 13.42 |
| Solution heat-treated | 0.00 | 0.20 ± 0.08 | 2.85 ± 5.78 | 34.95 ± 11.30 |

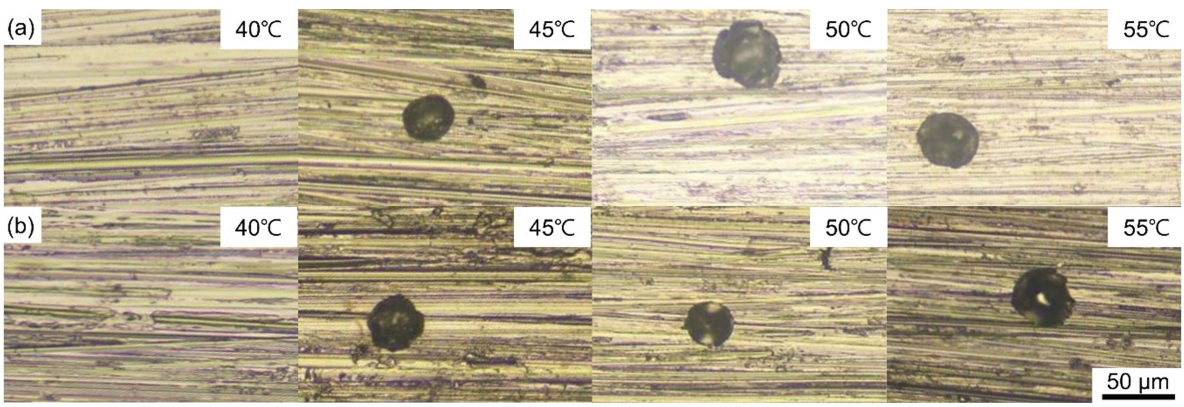


**Fig. 5. Optical microscopic images after the immersion test of (a) as-hot-rolled (b) solution heat-treated UNS N07718 alloys at 40, 45, 50, and 55 °C for 72 h**

where $W$ is the mass loss value after the immersion (mg), $D$ is the density (g $cm^{-1}$), $A$ is the surface area of the alloy ($in^2$), and $T$ is the immersion time (h). No mass loss occurs at immersion temperatures of 35 and 40 °C, irrespective of the heat treatment. The corrosion rate increases as the immersion temperature increases from 45 to 55 °C, and the rates for the as-hot-rolled condition are at least three times higher than those for the solution-heat treated alloy, suggesting that localized corrosion resistance is enhanced when the as-hot-rolled alloy undergoes solution heat treatment at 1050 °C for 2.5 hours.

Fig. 5 presents optical microscopic images taken after immersion tests for UNS N07718 alloy in both (a) as-hot-rolled and (b) solution-heat-treated conditions. Regardless of the heat treatment, corrosion featuring a circular shape at the opening mouth is observed on the alloy surfaces when immersion temperatures exceed 45 °C. Fig. 6 depicts the cross-sectional profiles of pit depths, as examined by a laser microscope for both (a) as-hot-rolled and (b) solution-heat-treated alloys. The pit morphology is similar to a pothole, displaying comparable depth and width. The pits' diameters range from 30 to

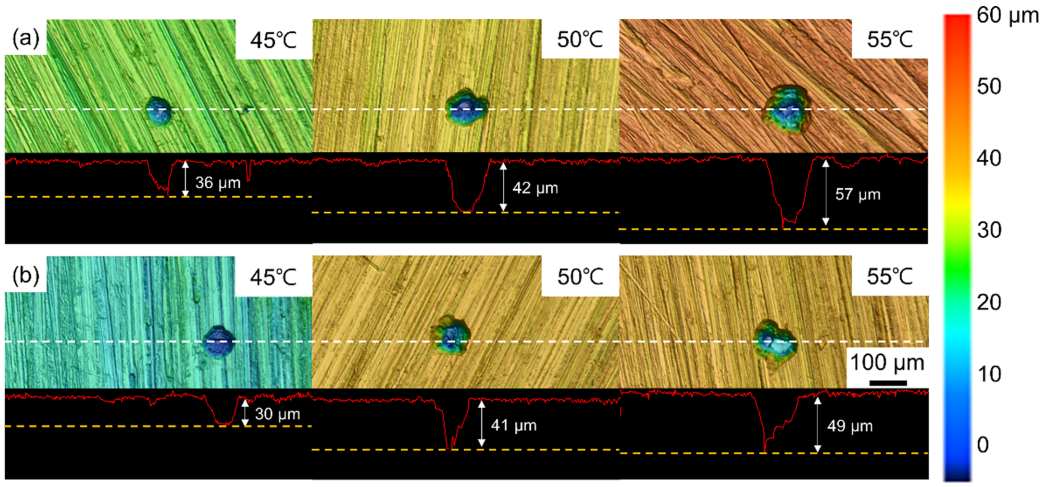


**Fig. 6. Confocal laser scanner microscopic images after the immersion test at 45, 50, and 55 °C for 72 h (a) as-hot-rolled (b) solution heat-treated UNS N07718 alloys**

**Table 3. The maximum depth (μm) and number of pits per square inch of two types of UNS N07718 alloys after undergoing an immersion test at 35, 40, 45, 50, and 55 °C for 72 hours**

| Temperature (°C) | | 35 | 40 | 45 | 50 | 55 |
|---|---|---|---|---|---|---|
| As-hot-rolled | Maximum depth (μm) | 0 | 0 | 37.0 ± 3.2 | 44.9 ± 6.1 | 53.9 ± 5.2 |
| | Number of pits/area ($in^2$) | 0 | 0 | 1007.0 ± 143.9 | 1035.8 ± 211.2 | 1286.1 ± 380.7 |
| Solution heat-treated | Maximum depth (μm) | 0 | 0 | 33.1 ± 6.7 | 42.4 ± 4.3 | 50.0 ± 5.6 |
| | Number of pits/area ($in^2$) | 0 | 0 | 863.1 ± 143.9 | 1007.0 ± 269.1 | 1194.0 ± 422.1 |

40 μm, and their maximum depths increase from approximately 35 to 50 μm as immersion temperatures rise from 45 to 55 °C (Table 2). This observation indicates that higher immersion temperatures lead to wider and deeper pits. Furthermore, pit propagation appears to be mitigated when the alloy undergoes solution heat treatment.

Table 3 presents the maximum pit depths and number of pits per square inch for two types of UNS N07718 alloys following a 72-hour immersion test. At an immersion temperature of 45 °C, the maximum pit depths for as-hot-rolled and solution heat-treated UNS N07718 alloys measure approximately 37.0 μm and 33.1 μm, respectively. As the critical pitting temperature, defined by the ASTM G-48 C-method [17], represents the minimum temperature needed to produce localized corrosion at least 25 μm deep on the specimen's surface, both types of UNS N07718 alloys share a critical pitting temperature of 45 °C. When the solution temperature rises from 45 to 55 °C, the maximum pit depth for as-hot-rolled UNS N07718 increases from 37.0 to 53.9 μm. Similarly, the maximum pit depth for solution heat-treated UNS N07718 rises from 33.1 to 50.0 μm as the solution temperature increases from 45 and 55 °C. At each immersion temperature, the as-hot-rolled UNS N07718 alloy exhibits a greater maximum pit depth than the solution heat-treated UNS N07718 alloy. Moreover, as the solution temperature elevates from 45 to 55 °C, the number of pits per square inch increases in both alloys. The as-hot-rolled UNS N07718 alloy features a higher number of pits per square inch than the solution heat-treated UNS N07718 alloy, indicating that localized corrosion is suppressed when the alloy undergoes solution heat treatment.

Fig. 7 displays optical microscopic images of mirror-polished, as-hot-rolled (a) and solution-heat-treated (b) UNS N07718 alloys after immersion tests at 50 °C for 24 hours. Localized corrosion in the form of pothole-shaped pits is observed near the nitrides. These nitrides have an approximate diameter of 10 μm and are likely Ti-rich, based on Fig.s 4 and 5. The pit width in the as-hot-rolled alloy is around 50 μm, while in the solution-heat-treated

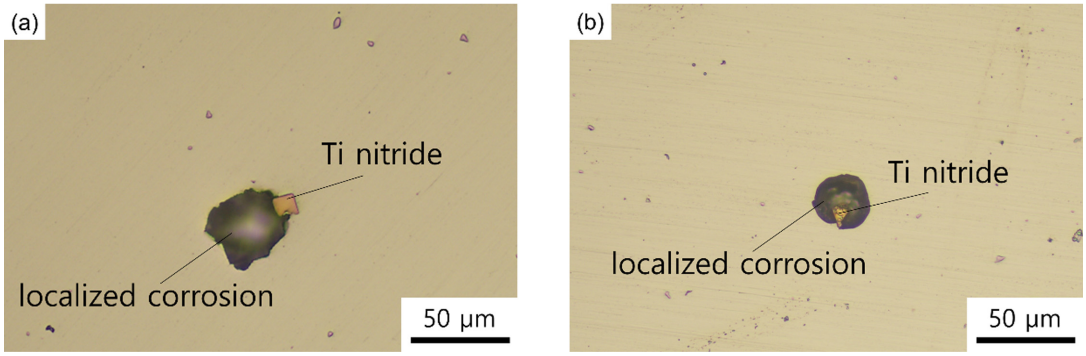


**Fig. 7. Optical microscopic images after the immersion test of (a) as-hot-rolled (b) solution heat-treated UNS N07718 alloys at 50 °C for 24 h**

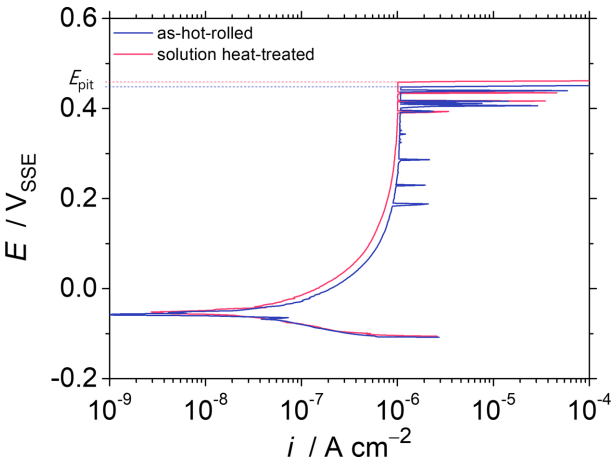


**Fig. 8. Potentiodynamic polarization curves of the UNS N07718 electrodes in 25 wt% NaCl + 0.5 wt% acetic acid at 50 °C**

alloy, it is approximately 30 μm. This suggests that localized corrosion occurs at the interface between the particles and the substrate. As previously reported, UNS N07718's localized corrosion is more likely to initiate at the Ti-carbide/substrate interface than the Nb-carbide/substrate interface due to the electrochemical nobility of Ti-carbide over Nb-carbide [9].

Fig. 8 shows potentiodynamic polarization curves for as-hot-rolled and solution heat-treated UNS N07718 alloys in 25 wt% NaCl and 0.5 wt% acetic acid at 50 °C. As the curves do not exhibit an active-to-passive transition, the alloy surfaces are in a passive state within the solution. The corrosion potential is nearly consistent even after heat treatment. A current that maintains passivity flows on the alloy surfaces during anodic polarization above the corrosion potential. The current values of 1 μA cm$^{-2}$ for as-hot-rolled surfaces and 0.9 μA cm$^{-2}$ for heat-treated surfaces at 0.3 V$_{SSE}$. However, current spikes arise during polarization from 0.188 to 0.440 V$_{SSE}$ and from 0.393 to 0.435 V$_{SSE}$ for as-hot-rolled and heat-treated surfaces, respectively. These current spikes indicate the initiation of metastable pits on the alloy surfaces. At potential values exceeding 0.454 or 0.465 V$_{SSE}$ for as-hot-rolled and heat-treated surfaces, respectively, the anodic current sharply rises and reaches 1 mA cm$^{-2}$. At this pitting potential, stable pits initiate or propagate on the alloy surfaces. Given that the as-hot-rolled alloy is more susceptible to metastable and stable pitting events than the solution heat-treated alloy, the solution heat-treatment process enhances the localized corrosion resistance of UNS N07718 alloy.

It is widely known that the initiation sites of localized corrosion in alloys are associated with their heterogeneous microstructure. In the case of UNS N07718 alloy, the primary MCs have been reported to be one of the initiation sites for localized corrosion in the alloy [9]. Though there are likely many initiation sites for localized corrosion in UNS N07718 alloy, such as grain boundaries, precipitates, or intermetallic phases, there has been, unfortunately, limited information reported on the initiation behavior of localized corrosion in these heterogeneous microstructures of the alloy.

On one hand, grain boundaries serve as potential localized corrosion initiation sites due to their atomic disordered two-dimensional defects, which possess higher surface energy than internal grains [27]. Frankel et al. proposed that localized corrosion occurred at grain boundaries because oxide regions along these boundaries had a lower resistance to ionic transport, making them the primary sites for oxide breakdown [28]. Markus et al. suggested that local thinning and an increased rate of ionic

transfer through grain boundaries occur due to potential redistribution [29].

On the other hand, localized corrosion at the grain boundaries in UNS N07718 is attributed to the presence of the δ phase. Groh et al. demonstrated that localized corrosion occurred within the δ phase ($Ni_3Nb$) in UNS N07718 [30]. Fig. 9 displays the secondary electron image and elemental mapping image of the UNS N07718 alloy after immersion in Kalling's No. 2 solution etchant. The grain boundaries, characterized by a three-grain interface and the needle-shaped bright phase, are identified. The needle-like phase has a width of a few nanometers and a length of approximately 3 μm at the grain boundary. Elemental mapping reveals that the concentration of Nb is relatively higher than that of the intergrains. Since the δ phase is reported to have a $Ni_3Nb$ composition in grain boundaries [31], it is suggested that the enriched needle-shaped phase could be the δ phase formed at the grain boundary. The number of delta phases per unit area of the specimen (in $\mu m^2$) is 0.121, and the number of delta phases corresponding to the number of carbides or nitrides is 0.163.

Fig. 10 presents optical microscopic images, topographical images, height line profiles, contact potential difference (CPD) images and CPD line profiles of (a) Nb carbide and (b) Ti nitride for as-hot-rolled UNS N07718 obtained from SKPFM. Brighter particles on the substrate and in the grain boundaries are evident in the topographical image of Fig. 10. The height line profile in Fig. 10(a) displays the delta phases in the grain boundary and Nb-Mo carbide with heights of approximately 0.04 and 0.24 μm, respectively. The height line profile in Fig. 10(b) shows the delta phase and Ti nitride with heights of

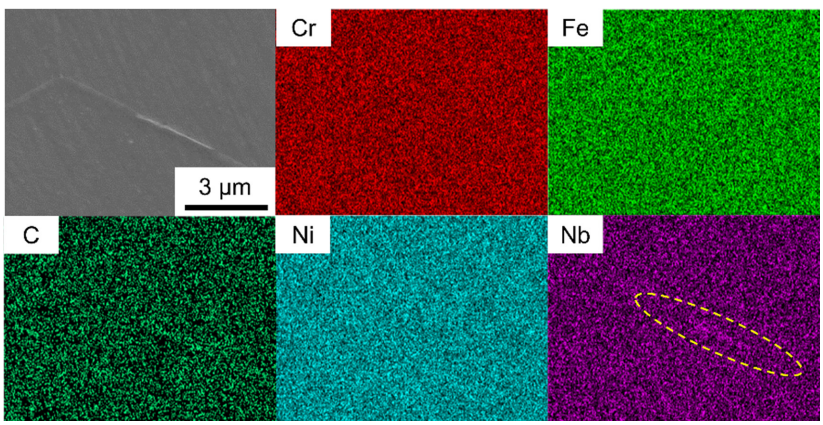


**Fig. 9. EDS elemental mapping images at a grain boundary of the as-hot-rolled UNS N07718 alloy**

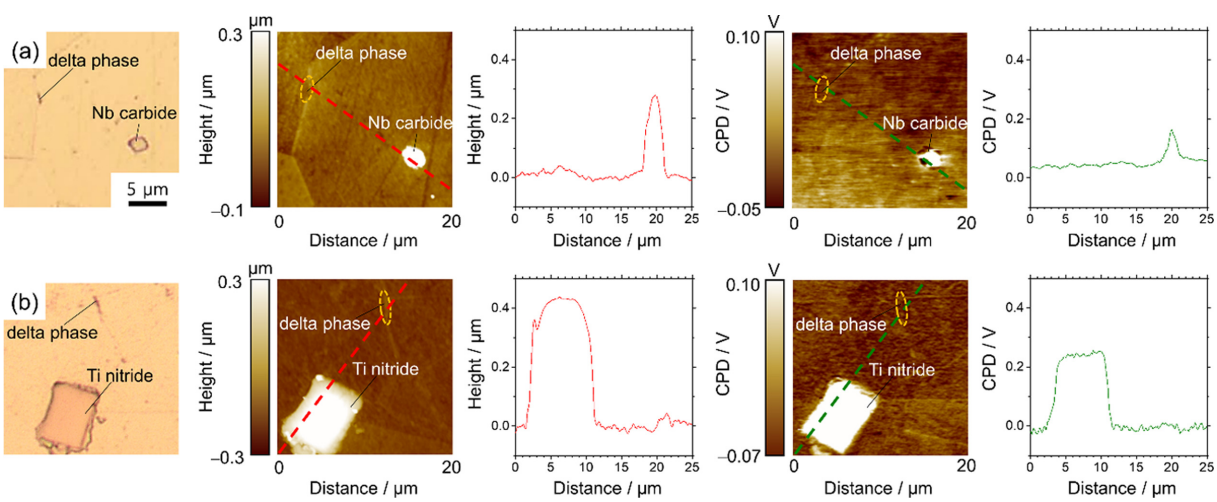


**Fig. 10. Optical microscopic, topographical images, height line profile, contact potential difference (CPD) images and CPD line profile of (a) Nb carbide and (b) Ti nitride with delta phases for as-hot-rolled UNS N07718 alloy**

approximately 0.06 and 0.43 μm, respectively. This variation can be attributed to the difference in hardness between the delta phase, Nb-Mo carbides, Ti nitrides, and the substrate [12,32,33]. The CPD values between the cantilever tip and the Nb-Mo carbide, and between the cantilever tip and Ti nitrides, are higher than those with the substrate. However, the CPD values between the cantilever tip and the delta phase are lower than that of the substrate. The $\Delta mV/V_0$ values for the delta phase, Nb-Mo carbide, and Ti nitride with respect to the substrate are approximately -1.26, 5.25, and 19, respectively. $V_0$ is the average value of CPD for substrate. $\Delta mV$ is difference the value of CPD between the substrate and delta phase, Nb-Mo carbide or Ti nitride. It is suggested that the delta phase and Nb-Mo carbide or Ti nitride may act as localized anodic and cathodic regions, respectively, relative to the substrate.

The strength of metallic bonds is relatively lower compared to ionic and covalent bonds, and a metallic bond is significantly influenced by the electron work function [34]. The work functions of Ti nitride and Nb carbide are 4.2 - 4.5 eV and 4.85 - 4.95 eV, respectively [35,36]. According to a previous study, the contact potential difference increases as the electron work function decreases [37]. Therefore, the CPD value of Ti nitride is higher than that of Nb-Mo carbide. Fig. 10 shows that the CPD profile of Ti nitride is higher compared to that of Nb-Mo carbide, suggesting that Ti nitride can be more electrochemically noble relative to Nb-Mo carbide. The CPD values of the delta phase, as shown in Fig. 10, are relatively consistent compared to the substrate. The delta phase may not strongly affect the initiation site of localized corrosion. This result implies that the substrate near the Ti nitride, which exhibits the highest CPD values compared to the substrate, will primarily act as the initiation site of localized corrosion for both types of UNS N07718. Therefore, the delta phase may not significantly influence the difference in localized corrosion resistance between the two types of UNS N07718.

In this study, grain coarsening occurred during the solution heat treatment, resulting in a reduced grain boundary area and the dissolution of the δ phases at grain boundaries. Additionally, the solution heat treatment is thought to decrease local compositional segregation. Tajyar et al. found that compositional segregation was eliminated when the UNS N07718 alloy underwent solution heat treatment [38]. Tucho et al. also found that solution annealing heat treatment reduced both micro and macro segregation in additively manufactured UNS N07718 [12]. This indicates that more compositionally homogeneous microstructures can potentially suppress the initiation of localized corrosion in UNS N07718 alloy. This study is the first to investigate the effect of solution annealing heat treatment on the localized corrosion resistance of UNS N07718 alloy, due to grain coarsening and compositional consistency of the MCs following the treatment. The information obtained from the primary heat treatments for UNS N07718 alloy provides a fundamental understanding of the mechanical and corrosion-resistant changes during secondary aging heat treatment. In the near future, the authors plan to present the localized corrosion resistance behavior of the alloy during the aging process.

## 4. Conclusion

The effects of solution heat treatment on the localized corrosion resistance of UNS N07718 alloy were examined using immersion tests in a 6 wt% $FeCl_3$ + 1.0 wt% HCl solution and electrochemical experiments in a 25 wt% NaCl + 0.5 wt% acetic acid solution. The average grain diameter increased, and the delta phases at grain boundaries dissolved into the matrix when the as-hot-rolled UNS N07718 alloy underwent solution heat treatment at 1050 ºC for 2.5 hours. The primary metallic nitrides (MN) and carbides (MC), predominantly composed of Ti or Nb-based materials, were randomly distributed on the specimen surfaces. Despite the solution heat treatment, the shape, composition, and frequency distribution of particle diameters remained similar between the as-hot-rolled and solution heat-treated UNS N07718 alloy. After the immersion test at 45 ºC, localized corrosion was observed, and the critical pitting temperature was determined to be 45 ºC for both types of UNS N07718 alloys. Following the solution heat treatment, the corrosion rate, maximum pit depth, and number of pits per unit area decreased at each immersion temperature in the acidic solution. Additionally, the pitting potential increased slightly, while current spikes arise at more noble potential. These microstructural changes are believed to

contribute to a more compositionally homogeneous microstructure, potentially reducing the onset of localized corrosion in the UNS N07718 alloy.

## Acknowledgements

This work was supported by Korea Institute of Energy Technology Evaluation and Planning (KETEP) grant funded by the Korea government (MOTIE) (20214000000480, Development of R&D engineers for combined cycle power plant technologies).

## References

1. C. M. Kuo, Y. T. Yang, H. Y. Bor, C. N. Wei, and C. C. Tai, Aging effects on the microstructure and creep behavior of Inconel 718 superalloy, *Materials Science and Engineering: A*, **510**, 289 (2009). Doi: https://doi.org/10.1016/j.msea.2008.04.097
2. E. Ott, X. Liu, J. Andersson, Z. Bi, K. Bockenstedt, I. Dempster, and C. Sudbrack, Ott, Proceedings of the 9th International Symposium on Superalloy 718 & Derivatives: Energy, Aerospace, and Industrial Applications, Springer (2018).
3. T. Trosch, J. Strößner, R. Völkl, and U. Glatzel, Microstructure and mechanical properties of selective laser melted Inconel 718 compared to forging and casting, *Materials letters,* **164**, 428 (2016). Doi: https://doi.org/10.1016/j.matlet.2015.10.136
4. H. S. Klapper, and J. Stevens, Susceptibility to pitting corrosion of nickel-based Alloy 718 exposed to simulated drilling environments, *Corrosion* **70**, 899 (2014). Doi: https://doi.org/10.5006/1154
5. U. Martin, J. Ress, J. Bosch, and D. M. Bastidas, Evaluation of the DOS by DL− EPR of UNSM Processed Inconel 718, *Metals,* **10**, 204 (2020). Doi: https://doi.org/10.3390/met10020204
6. F. Andreatta, I. Apachitei, A. A. Kodentsov, J. Dzwonczyk, and J. Duszczyk, Volta potential of second phase particles in extruded AZ80 magnesium alloy, *Electrochimica Acta,* **51**, 3551 (2006). Doi: https://doi.org/10.1016/j.electacta.2005.10.010
7. S. Rahman, G. Priyadarshan, K. S. Raja, C. Nesbitt, and M. Misra, Investigation of the secondary phases of alloy 617 by scanning kelvin probe force microscope, *Materials Letters,* **62**, 2263 (2008). Doi: https://doi.org/10.1016/j.matlet.2007.11.077
8. J.-S. Lee, Y.-J. Lee, S. I. Kwon, J. Shin, and J.-H. Lee, Localized Corrosion Behavior of Inconel 718 in a Chloride-Containing Aqueous Solution, *Corrosion Science and Technology,* **20**, 361 (2021). Doi: https://doi.org/10.14773/cst.2021.20.6.361
9. J.-S. Lee, Y.-J. Lee, S. I. Kwon, J. Shin, Y. T. Cho, S. Kim, and J.-H. Lee, Localized Corrosion Behavior of UNS N07718 in a Solution Simulating a Diluted-sour Environment, *Korean Journal of Metals and Materials,* **61**, 553 (2023). Doi: http://dx.doi.org/10.3365/KJMM.2023.61.8.553
10. G. A. Rao, M. Kumar, M. Srinivas, and D. S. Sarma, Effect of standard heat treatment on the microstructure and mechanical properties of hot isostatically pressed superalloy inconel 718, *Materials Science and Engineering: A,* **355**, 114 (2003). Doi: https://doi.org/10.1016/S0921-5093(03)00079-0
11. X. L.An, L. Zhou, B. Zhang, C. L. Chu, L. Y.Han, and P. K. Chu, Inconel 718 treated with two-stage solution and aging processes: microstructure evolution and enhanced properties, *Materials Research Express,* **6**, 075803 (2019). Doi: https://doi.org/10.1088/2053-1591/ab1290
12. W. M. Tucho, P. Cuvillier, A. Sjolyst-Kverneland, and V. Hansen, Microstructure and hardness studies of Inconel 718 manufactured by selective laser melting before and after solution heat treatment, *Materials Science and Engineering: A,* **689**, 220 (2017). Doi: https://doi.org/10.1016/j.msea.2017.02.062
13. J. Rosenberg, J. Klower, J. Groth, C. Bosch, and G. Genchev, *Proc. NACE CORROSION Conf.*, Paper No. NACE 10650 (2018).
14. R. Rebak, M. Rincón-Ortíz, M. Iannuzzi, M. Kappes, A. Mishra, and M. Rodriguez, Effect of thermal treatment on the localized corrosion behavior of alloy 718 (UNS N07718), European Federation of Corrosion, (2014). Doi: http://hdl.handle.net/20.500.11937/75302
15. L. C. M. Valle, A. I. C. Santana, M. C. Rezende, J. Dille, O. R. Mattos, and L. H. de Almeida, The influence of heat treatments on the corrosion behaviour of nickel-based alloy 718, *Journal of Alloys and Compounds,* **809**, 151781 (2019). Doi: https://doi.org/10.1016/j.jallcom.2019.151781
16. ASTM E112-96, Standard test methods for determining average grain size, ASTM International, West Conshohocken, PA, USA (2004).
17. ASTM G48-03, Standard Test Methods for Pitting and Crevice Corrosion Resistance of Stainless Steels and Related Alloys by Use of Ferric Chloride Solution, ASTM International (2009).
18. F. da Cruz Gallo, L. M. B. de Azevedo, C. Labre, L. S. Araujo, J. Dille, and L. H. de Almeida, Correlation between grain boundary character distribution and δ-

phase precipitation in nickel-based superalloy 718, *Journal of Materials Research and Technology,* **9**, 1801 (2020). Doi: https://doi.org/10.1016/j.jmrt.2019.12.011

19. A. R. Figueiredo, L. M. B. de Azevedo, F. da Cruz Gallo, M. A. R. Medeiros, L. H. de Almeida, L. S. Araújo, and A. da Cunha Rocha, Effect of annealing twins, strain-recrystallization processing and δ-phase fraction on micro-texture and evaluation of mechanical properties of nickel-based superalloy 718, *Materials Science and Engineering: A,* 145341 (2023). Doi: https://doi.org/10.1016/j.msea.2023.145341
20. V. Beaubois, J. Huez, S. Coste, O. Brucelle, and J. Lacaze, Short term precipitation kinetics of delta phase in strain free Inconel* 718 alloy, *Materials Science and Technology,* **20**, 1019 (2004). Doi: https://doi.org/10.1179/026708304225019830
21. L. C. M. Valle, L. S. Araújo, S. B. Gabriel, J. Dille, and L. H De Almeida, The effect of δ phase on the mechanical properties of an Inconel 718 superalloy, *Journal of materials engineering and performance,* **22**, 1512 (2013). Doi: https://link.springer.com/article/10.1007/s11665-012-0433-7
22. K. Wilkinson, J. Lundkvist, G. Seisenbaeva, and V. Kessler, New tabletop SEM-EDS-based approach for cost-efficient monitoring of airborne particulate matter, *Environmental pollution,* **159**, 311 (2011). Doi: https://doi.org/10.1016/j.envpol.2010.08.024
23. G. K. Dosbaeva, S. C. Veldhuis, A. Elfizy, G. Fox-Rabinovich, and T. Wagg, Microscopic observations on the origin of defects during machining of direct aged (DA) Inconel 718 superalloy, *Journal of Materials Engineering and Performance,* **19**, 1193 (2010). Doi: https://link.springer.com/article/10.1007/s11665-009-9587-3
24. T. Zaman, M. Farooque, S. A. Rizvi, I. Salam, and M. Waseem, Investigation of low stress rupture properties in Inconel-718 super alloy, *IOP Conference Series: Materials Science and Engineering,* **146**, 012051 (2016). Doi: https://doi.org/10.1088/1757-899X/146/1/012051
25. P. Hoier, A. Malakizadi, P. Stuppa, S. Cedergren, and U. Klement, Microstructural characteristics of Alloy 718 and Waspaloy and their influence on flank wear during turning, *Wear,* **400**, 184 (2018). Doi: https://doi.org/10.1016/j.wear.2018.01.011
26. ASTM G31-72, Standard Practice for Laboratory Immersion Corrosion Testing of Metals, ASTM, PA, USA (2004). https://www.astm.org/g0031-72r04.html
27. B. W. Bennett, and H. W. Pickering, Effect of grain boundary structure on sensitization and corrosion of stainless steel, *Metallurgical and Materials Transactions A,* **18**, 1117 (1987). Doi: https://link.springer.com/article/10.1007/BF02668561
28. G. S. Frankel, and N. Sridhar, Understanding localized corrosion, *Materials today,* **11**, 38 (2008). Doi: https://doi.org/10.1016/S1369-7021(08)70206-2
29. P. Marcus, V. Maurice, and H. H. Strehblow, Localized corrosion (pitting): A model of passivity breakdown including the role of the oxide layer nanostructure, *Corrosion science,* **50**, 2698 (2008). Doi: https://doi.org/10.1016/j.corsci.2008.06.047
30. J. R. Groh, R. W. Duvelius, and L. A, Influence of corrosion pitting on alloy 718 fatigue capability, *Superalloy 718,* 583 (2001). Doi: https://www.tms.org/superalloys/10.7449/2001/superalloys_2001_583_592.pdf
31. S. Azadian, L. Y. Wei, and R. Warren, Delta phase precipitation in Inconel 718, *Materials characterization,* **53**, 7 (2004). Doi: https://doi.org/10.1016/j.matchar.2004.07.004
32. S. G. Huang, K. Vanmeensel, H. Mohrbacher, M. Woydt, and J. Vleugels, Microstructure and mechanical properties of NbC-matrix hardmetals with secondary carbide addition and different metal binders, *International Journal of Refractory Metals and Hard Materials*, **48**, 418 (2015). Doi: https://doi.org/10.1016/j.ijrmhm.2014.10.014
33. D. S. Stone, K. B. Yoder, and W. D. Sproul, Hardness and elastic modulus of TiN based on continuous indentation technique and new correlation, *Journal of Vacuum Science & Technology A: Vacuum, Surfaces, and Films,* **9**, 2543 (1991). Doi: https://doi.org/10.1116/1.577270
34. J. Cui, L. Guo, H. Lu, and D. Y. Li, Understanding effects of Cr content on the slurry erosion behavior of high-Cr cast irons through local property mapping and computational analysis, *Wear*, **376**, 587 (2017). Doi: https://doi.org/10.1016/j.wear.2016.12.031
35. S. A. Vitale, J. Kedzierski, P. Healey, P. W. Wyatt, and C. L. Keast, Work-function-tuned TiN metal gate FDSOI transistors for subthreshold operation, *IEEE Transactions on Electron Devices*, **58**, 419 (2010). Doi: https://doi.org/10.1109/TED.2010.2092779
36. R. Fujii, Y. Gotoh, M. Y. Liao, H. Tsuji, and J. Ishikawa, Work function measurement of transition metal nitride and carbide thin films, *Vacuum*, **80**, 832 (2006). Doi: https://doi.org/10.1016/j.vacuum.2005.11.030
37. M. Yoshitake, Y. Aparna, and K. Yoshihara, Tailoring of work function by surface segregation, *Applied surface science*, **169**, 666 (2001). Doi: https://doi.org/10.1016/

S0169-4332(00)00809-6

38. A. Tajyar, N. Brooks, N. Holtham, R. Rowe, D. J. Newell, A. N. Palazotto, and K. Davami, Effects of a modified heat-treatment on microstructure and mechanical properties of additively manufactured Inconel 718, *Materials Science and Engineering: A,* **838**, 142770 (2022). Doi: https://doi.org/10.1016/j.msea.2022.142770